Special Feature: Vehicle Engineering

Study on Roller Behavior and Thrust Force of Tripod Constant Velocity Joint

Hideki Sugiura, Yoshiteru Mizutani, Tsugiharu Matsunaga, Yosei Ando and Isashi Kashiwagi

Report received on Sep. 18, 2012

■**ABSTRACT**‖ Tripod constant velocity joints are used in the driveshaft of front wheel drive vehicles. Thrust force generated by this joint causes lateral vibration in these vehicles. To determine the mechanisms inducing the thrust force, a detailed model is constructed based on a multibody dynamics approach. Although the joint is equipped with three rollers and grooves, this model consists of the principal parts for one roller and groove in order to precisely analyze frictional phenomena occurring between the roller and the groove. To simulate the actual behavior of the one roller, the relative motions between the groove and the trunnion supporting the roller are formularized and applied as driving constraints. These principal parts are defined as rigid bodies and are connected by force elements of contact and friction. The appropriateness of this model is validated by comparing computational and experimental results. The experimental apparatus is also constructed using one roller and groove of the actual joint. As the result, it is clarified that the principal factors inducing the thrust force are three kinds of sliding friction force at the point of contact between the roller and the groove. This paper also describes the reason why the third rotating order component of the thrust force is induced by one roller and groove.

■**KEYWORDS**‖ Multibody Dynamics, Tripod Joint, Constant Velocity Joint, Roller Behavior, Thrust Force, Friction Force

1. Introduction

A constant velocity joint transmits driving torque when a joint angle exists between two transmitting axes. A tripod constant velocity joint, which is used as an axle driveshaft inboard joint in front wheel drive vehicles, also has a plunging mechanism permitting axial displacement. However this useful function also generates housing axial thrust force whose amplitude periodically changes with the revolution of the driveshaft. In order to reduce this dynamic force, which induces lateral vibration in the vehicle, it is necessary to develop a computational method for this force and to clarify the factors causing it. These are longstanding problems because it is very difficult to deal with dynamic contact and friction between multiple parts.

With respect to these problems, a detailed analysis model was constructed that included contact and friction forces acting among multiple parts of the joint, based on a multibody dynamics approach, and a parameter study into contact regions and friction forces showed quantitatively that sliding friction between a spherical roller and a groove caused the principal component of the thrust force (the third rotating order component).[1] However, in order to clarify the fundamental factors inducing the thrust force and to reduce the thrust force, it is necessary to identify the mechanism that induces sliding friction between the roller and the groove.

This paper describes the frictional phenomena occurring between the roller and the groove. Although a tripod constant velocity joint is equipped with three rollers and grooves, the analysis model is constructed using the principal parts for one roller and groove in order to simulate these complicated phenomena appropriately. To ensure that the behavior of the one roller in this model simulates the actual behavior of the joint, relative motions between the groove and the trunnion supporting the spherical roller are formularized. By performing multibody dynamics analysis including these formulas as driving constraints, the roller behavior based on contact and friction is derived. Moreover, the principal factors that generate sliding friction of the roller are identified, and the reason inducing the third rotating order component

of the thrust force is clarified. This paper also describes the appropriateness of the analysis model. This model is validated by comparing computational and experimental results in the case of one roller and groove.

2. Analysis Model

2. 1 Mechanism of Tripod Constant Velocity Joint

Figure 1 shows the tripod constant velocity joint. The housing acts as the input axis and includes three equally spaced grooves. The direction of these grooves is parallel to the input shaft. Each groove is configured as a half circular cylinder. The intermediate shaft acts as the output axis. The spider, which consists of three equally spaced trunnions, is connected to this shaft. The spherical roller is supported on the trunnion through multiple needle rollers. Driving torque is transmitted between the grooves of the input side and the spherical rollers of the output side.

2. 2 Relative Motions of Trunnion to Groove

The joint is assumed to be in an actual condition where lateral vibration of a vehicle is induced (especially in a case of acceleration). The housing of the input axis transmits driving torque to the intermediate shaft of the output axis in the same direction as the revolving direction. Here, the coordinate system in this section is based on the coordinates of the input axis shown in **Fig. 2**. In the case where the revolving direction of the joint is counterclockwise, the output axis also whirls clockwise. While this output axis whirls conically once, the trunnion and the roller go back and forth in the groove once and the spider center revolves eccentrically around the joint center twice.[2] From the viewpoint of the output

axis, the locus of the spider center is circular and the direction of this revolution is the same as the revolution of the joint.[3] Utilizing these facts, the behavior of the trunnion is formularized in the following sections. Here the revolution around the x axis of the trunnion is called "pitching". In the same way, revolution in the y axis is called "yawing" and revolution in the z axis is called "rolling".

2. 2. 1 Pitching

The pitching angle φ of the trunnion is obtained based on the conical whirl of the output axis as shown in **Fig. 3**. This angle is defined by

$$\tan\varphi = R\sin\omega t \,/\, L = \tan\theta\,\sin\omega t \,, \quad\cdots\cdots\cdots (1)$$

where θ is the joint angle, ω is the angular velocity of the conical whirl of the output axis, t is the time, R is the radius of the conical whirl at the output axis end and L is the length of the z direction at the output axis end. R and L are variables for θ. In a case where φ and θ are considered to be small values, Eq. (1) is approximated as follows.

$$\varphi = \theta\sin\omega t \cdots\cdots\cdots\cdots\cdots\cdots\cdots\cdots (2)$$
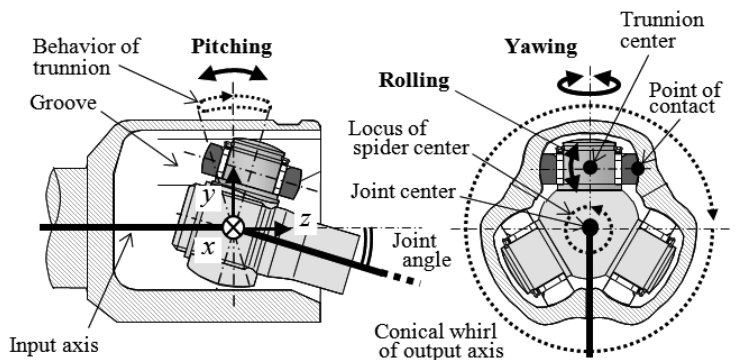

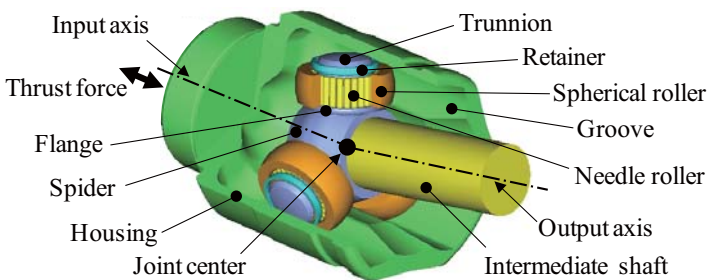**Fig. 2**   Schematic of relative motions.

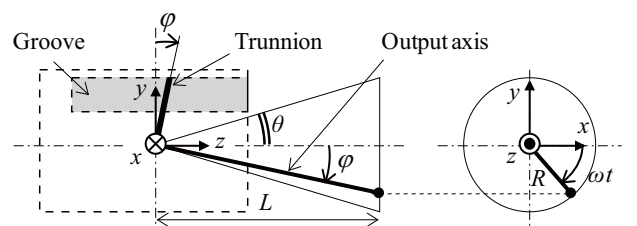**Fig. 1**   Tripod constant velocity joint.

Fig. 3   Schematic of pitching.

2. 2. 2 Yawing

The yawing angle ψ of the trunnion is also obtained based on the conical whirl of the output axis as shown in **Fig. 4**. This angle is defined by

$$\tan\psi = R\cos\omega t \, / \, L = \tan\theta \cos\omega t \, . \cdots \cdots \cdots (3)$$

In the same way as for pitching, Eq. (3) is approximated as follows.

$$\psi = \theta \cos\omega t \, \cdots \cdots \cdots \cdots \cdots \cdots \cdots (4)$$

2. 2. 3 Rolling and Axial Displacement of Trunnion

The behavior of the trunnion, based on eccentric revolution of the spider center, is composed of the rolling motion and the axial displacement of the trunnion. Here, since the roller supported by the trunnion is always pressed into the groove during transmission of load, the displacement of the trunnion center (shown in Fig. 2) is assumed to be toward the axial direction only. **Figure 5** shows the behavior of the spider center and the trunnion center at the coordinates of the output axis. The rolling angle ξ is defined by

$$\sin\xi = e\sin2\omega t \, / \, s \, , \, \cdots \cdots \cdots \cdots \cdots \cdots (5)$$

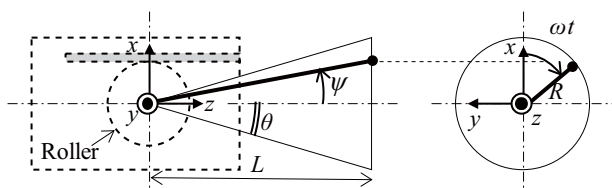where e is the eccentricity of the spider center and s is the distance between the spider center and the trunnion

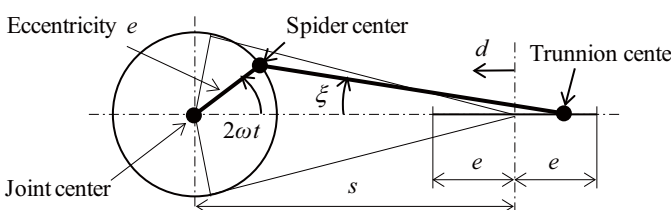center. Considering that ξ is a small value, and using the formula $e = s\,(1 - \cos\theta) \, / \, (2\cos\theta)$ based on Ref. (3), Eq. (5) is approximated as follows.

$$\xi = \frac{1 - \cos\theta}{2\cos\theta} \sin2\omega t \, \cdots \cdots \cdots \cdots \cdots \cdots (6)$$

Next, the axial displacement d of the trunnion is shown by

$$d = s - (e\cos2\omega t + s\cos\xi) \, . \, \cdots \cdots \cdots \cdots (7)$$

Using the approximation of $\cos\xi \approx 1$ in the case where ξ is a small value, Eq. (5) is shown as follows.

$$d = -\,e\cos2\omega t \, \cdots \cdots \cdots \cdots \cdots \cdots \cdots (8)$$

2. 3 Outline of Computational Method

Figure 6 shows a schematic of the analysis model, which consists of the principal parts for one roller and groove. These parts are defined as rigid bodies, which include both mass and inertia, and are located in a three-dimensional global coordinate system. A force element, which consists of contact force and friction force, connects each part, i.e., the groove in the housing, the spherical roller, the needle roller, and the trunnion on the spider. The clearance among these parts is considered based on the locations and contact configurations of the actual parts. Here, the groove is completely fixed to the ground of the global coordinate system, and the relative motions described in Section 2.2 are given between this groove and the trunnion as driving constraints.

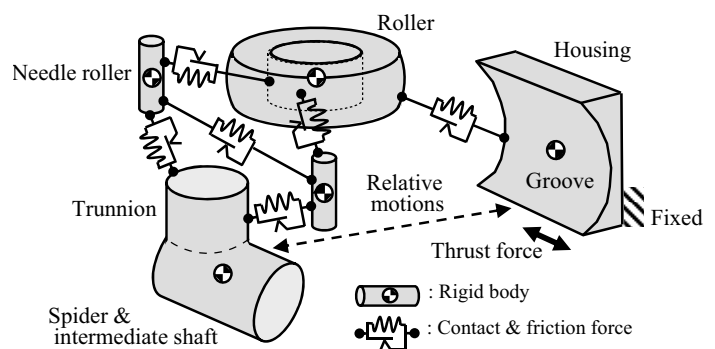The equations of motion in the multibody system are derived from this model. The equations can be

Fig. 4 Schematic of yawing.

Fig. 5 Schematic of rolling and displacement of axis direction of trunnion.

Fig. 6 Schematic of multibody model.

described as follows.[4]

$$\begin{bmatrix} \mathbf{M} & \mathbf{\Phi_q}^T \\ \mathbf{\Phi_q} & \mathbf{0} \end{bmatrix}\begin{bmatrix} \ddot{\mathbf{q}} \\ \lambda \end{bmatrix} = \begin{bmatrix} \mathbf{Q} \\ \gamma \end{bmatrix}, \cdots\cdots\cdots\cdots (9)$$

where $\mathbf{M}$ is the generalized mass matrix, $\ddot{\mathbf{q}}$ is the acceleration vector in the generalized coordinate system $\mathbf{q}$, $\mathbf{\Phi_q}$ is Jacobian and obtained by partial differentiation of the constraint equation $\mathbf{\Phi} \equiv \mathbf{\Phi}(\mathbf{q}, t) = 0$ based on $\mathbf{q}$ and time t, and $\mathbf{Q}$ is the generalized force vector, which consists of external forces (considering contact and friction force) and the terms of inertia using the square of angular velocity. γ is obtained by second order differentiation of $\mathbf{\Phi}$ as $\gamma \equiv \mathbf{\Phi_q}\ddot{\mathbf{q}} = -(\mathbf{\Phi_q}\dot{\mathbf{q}})_q \dot{\mathbf{q}} - 2\mathbf{\Phi_{qt}}\dot{\mathbf{q}} - \mathbf{\Phi_{tt}}$,

$\mathbf{\Phi_{qt}} = \left[\partial^2 \Phi_i / \partial q_j \partial t \right]_{nh \times nc}$, and $\mathbf{\Phi_{tt}} = \left[\partial^2 \Phi_i / \partial t^2 \right]_{nh \times 1}$,

where nh is the number of the holonomic constraint and nc is the number of the generalized coordinate system. These differential-algebraic equations of motion are solved and the thrust force is derived from the force which acts in the longitudinal direction of the groove.

In the actual analysis, the commercial software DADS [5] is utilized for developing the analysis model and solving the equations of motion numerically.

2. 4 Contact and Friction Model

Figure 7 shows a schematic diagram of the contact and friction model. When each contact surface attached on two rigid bodies overlaps, contact force derived from the penetration of this overlap acts on each point of contact of the two rigid bodies. If a relative velocity betw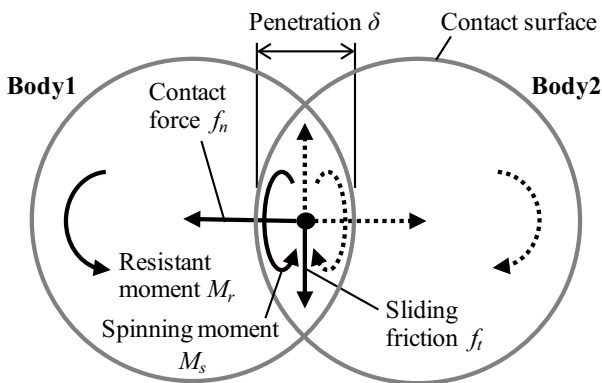een the two rigid bodies exists at the point of contact, friction force works toward the tangential direction. If a relative angular velocity between the two rigid bodies exists, spinning moment acts around the normal vector of the point of contact. Moreover, if rolling between the two bodies appears, rolling resistance moment is generated. These equations are described as follows.

The contact force f_n is the power of the penetration δ [mm] and defined by

$$f_n = C \delta^n, \cdots\cdots\cdots\cdots\cdots\cdots (10)$$

where n is the exponent of the power and C is the coefficient. These values are set up according to contact configuration.

The friction force f_t is derived from a multiplication of the contact force and the sliding friction coefficient μ_s and defined by

$$f_t = \mu_s f_n , \cdots\cdots\cdots\cdots\cdots\cdots (11)$$

where μ_s is the dynamic friction coefficient. Here, μ_s contains the hyperbolic tangent function shown in **Fig. 8** in order to model the friction force, which increases continuously from zero relative velocity.

The rolling resistance moment M_r can be discussed as follows. In a case where the resistance force F is generated by rolling a needle roller between two plates under load P, as shown in **Fig. 9**, the rolling friction coefficient is defined as $\mu_r = F / P$.[6] Here, the rolling resistance moment is derived from a multiplication of F and the diameter of the needle roller D. However, considering that this moment contains resistance concerning two points of contact, it is actually represented as follows.

$$M_r = F D / 2 = \mu_r P D / 2 \cdots\cdots\cdots\cdots (12)$$

μ_r also includes the hyperbolic tangent function.

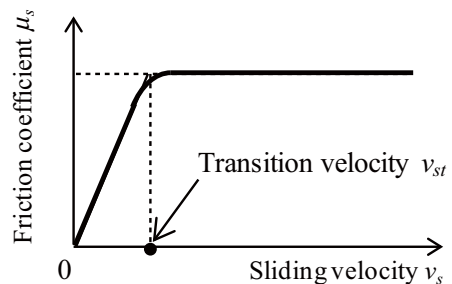**Fig. 7**　Schematic of contact model.

Fig. 8　Function of sliding friction coefficient.

The configuration of each contact region is explained in the following sections. It is also described how the exponent n and the coefficient C are obtained.

2. 4. 1 Contact between Spherical Roller and Groove

The contact surface of the roller is a sphere, and the contact surface of the groove is a half circular cylinder. Using the theory of elasticity by Hertz, the elastic penetration δ_{ro} [mm] is defined as follows.[7]

$$\delta_{ro} = 1.5 \frac{2K}{\pi\mu} \sqrt[3]{\frac{[1-(1/m^2)]^2}{3E^2} \Sigma\rho \cdot f_n^2} , \quad \cdots \cdots (13)$$

where ρ [1/mm] is the curvature of the contact surface and $2K/\pi\mu$ is the coefficient determined by the curvature. By converting this equation using Eq. (10) or the like, n and C are obtained as shown in **Table 1**.

This section also discusses the spinning moment M_s. The contact ellipse between the sphere and the cylinder has a ratio of 20 to 1. In the case where the major axis radius of the contact ellipse is $2a$ [mm], the spinning moment is approximated as follows.[8]

$$M_s = (3/8) \mu_s f_n a \cdots \cdots \cdots \cdots \cdots \cdots (14)$$

By using the coefficient μ based on the curvature of the contact surface in the theory by Hertz, a is defined
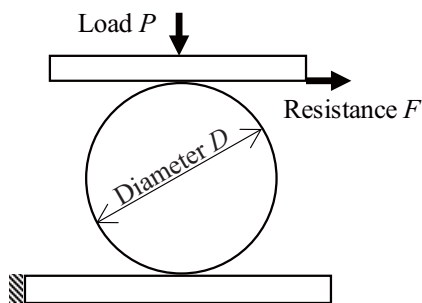
Fig. 9   Definition of rolling friction.

Table 1   Details of exponent n and coefficient C.

Object	Roller vs. groove	Needle roller vs. other parts
n	$3/2$	$10/9$
C	$\dfrac{0.942}{\sqrt{(2K/\pi\mu)^3 \Sigma\rho}} \dfrac{E}{1-(1/m^2)}$	$8.15 \times 10^4 \dfrac{l^{8/9}}{N_s}$

by the following equation.[7]

$$2a = 2\mu \sqrt[3]{\frac{3[1-(1/m^2)]}{E} \frac{f_n}{\Sigma\rho}} \quad \cdots \cdots \cdots \cdots (15)$$

M_s is therefore defined by

$$M_s = 0.541 \sqrt[3]{\frac{1-(1/m^2)}{E}} \frac{\mu}{\sqrt[3]{\Sigma\rho}} \mu_s f_n^{4/3} . \quad \cdots \cdots (16)$$

2. 4. 2 Contact between Needle Roller and Other Parts

The needle roller configured as a cylinder touches the trunnion, the inside surface of the spherical roller, and the next needle rollers located on both sides, respectively. These parts are also configured as a cylinder. Here, the analysis model of this paper takes the clearance among all parts into account, and the needle roller has six degrees of freedom. Several contact conditions therefore occur: equal line contact in the case of two parallel axes, unequal line contact in the case of two inclined axes, and point contact in the case of two skewed axes.

In order to efficiently simulate the multiple contact phenomena mentioned above, a new modeling method has been proposed that discretely approximates line contact using multiple point contacts.[1] In this model, N_s spherical configurations with the same diameter as the needle roller are prepared, and a contact surface is constructed that arranges these spheres in a line. The needle roller model is defined as a rigid body with the inertia of a cylinder and is equipped with this contact surface as shown in **Fig. 10**. Each spherical configuration touches three kinds of cylindrical contact surfaces: the trunnion, the inside of the spherical roller, and the next needle roller. The flange of the trunnion and the retainer on the trunnion are also modeled using contact elements to prevent the needle rollers from springing out. The total number of this needle roller model needs to be the same as the number of the needle rollers N_n, which is used on the trunnion, in order to construct the bearing.

Next, the contact force of each sphere is formulized. It is clarified that the elastic penetration δ_{ne} [mm] between two parallel cylinders is independent of the curvature of each cylinder and is dependent on the load and the length of the line contact.[9] Therefore, in the

case of steel, this is,

$$\delta_{ne} = 3.8 \times 10^{-5} \, (N_s f_n)^{0.9} / l^{0.8}, \cdots\cdots\cdots (17)$$

where f_n is the contact force on one sphere and l [mm] is the length of the contact region. The exponent n and the coefficient C, as shown in Table 1, can be obtained by converting this equation using Eq. (10) or the like.

3. Validation of Analysis Model

3. 1　Analysis Conditions

Compulsory displacement of the trunnion is applied to ensure the roller is pressed into the groove by a proper load value, and the relative motions shown in Section 2.2 are defined between the trunnion and the housing. With respect to validation of the model, pitching motion is applied that can be compared with experimental data. The initial value of the pressing load is 1000N, the whirling speed ω of the output axis is 20π rad/s (10Hz), and the joint angle is 10 degrees. The location and configuration of each part of the actual joint are utilized in the analysis model. This joint has forty-six needle rollers for one trunnion, i.e., $N_n = 46$. The number of spheres of one needle roller model is seven, i.e., $N_s = 7$. The Young's modulus and Poisson's ratio are the general values for the steel.

With respect to the friction coefficients, the sliding friction coefficient between the roller and the groove is 0.055, the sliding friction coefficient between the needle roller and other parts is 0.050, and the rolling friction coefficient is 0.002. These values were measured using greased test pieces. So that the friction force acts with a low relative velocity, the transition velocity v_{st}, that is, the criterion to change to a constant friction (shown in Fig. 8), is defined as one fourth of the maximum sliding velocity in the analysis results. The same rule is applied in the case of the rolling friction.
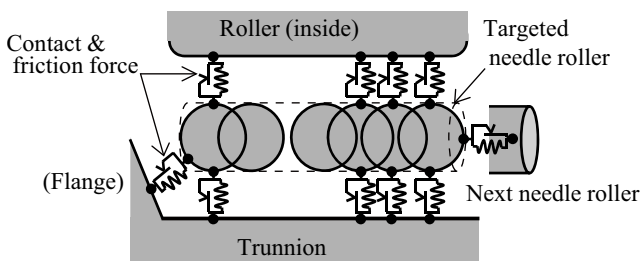

Fig. 10 Contact model set of needle roller.

3. 2　Analysis Results

The forces acting between the roller and the groove are defined using the coordinates of the input axis. The pressing force is F_x, the lateral force is F_y, and the thrust force is F_z. **Figure 11** shows two waveforms: the component ΔF_x fluctuating from the initial pressing value and F_y, with the position of both the roller and the trunnion. Next, **Fig. 12** shows F_z and the modified thrust force F_z'. Here, the results of the second cycle from the beginning of the analysis were used in these waveforms. In order to eliminate the influence of ΔF_x, F_z' is obtained by dividing F_z by F_x and multiplying this value by the initial pressing force for every time step of the analysis output. Since the characteristics of the waveform of F_z' hardly change from F_z, F_z' is used in following sections.

3. 3　Validation by Experiment

3. 3. 1　Outline of Apparatus

The experimental apparatus was constructed using actual parts of the joint. Using this apparatus, the forces acting on the groove were measured under the same conditions as the analysis. **Figure 13** shows an
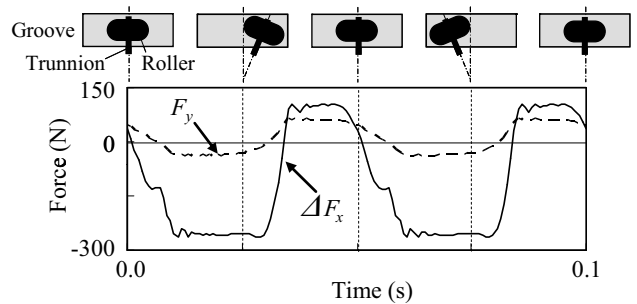

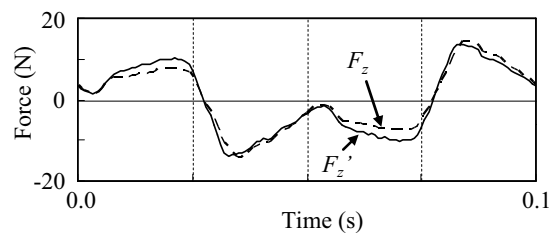**Fig. 11** Computational result of pressing force ΔF_x and lateral force F_y.

Fig. 12 Computational result of thrust force F_z and modified thrust force F_z'.

outline of the apparatus and details of the parts and the load sensor. The groove cut off the housing is fixed on the load sensor. This load sensor is a piezoelectric type and is able to measure three components, F_x, F_y, and F_z, individually. Since the trunnion has axial symmetry (cylindrical configuration), the spider is set to the groove turning around the trunnion axis by 90 degrees. The intermediate shaft connected to the spider is supported by bearings that allow rotating and sliding motions, and the other end of this shaft is loaded by a mechanical jack. The pitching motion is applied by oscillating the arm attached to the intermediate shaft.

3. 3. 2 Comparison of Experimental and Computational Results

Figure 14 shows ΔF_x and F_y of the experimental results. These are consistent with the phase of the oscillation of the computation. However, the amplitude of the computational ΔF_x is two times as large as the experimental result. This is thought to be due to the influence of elastic deformation of the apparatus. Although the stiffness of the intermediate shaft is considered by a beam element in the analysis model, the stiffness of the other parts that construct the
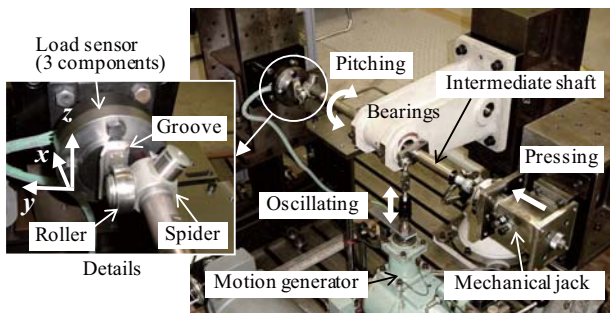
apparatus, such as steel blocks and the mechanical jack is not simulated. It is inferred that the rigid stiffness of these supporting parts causes the large fluctuation of the computational results.

Next, experimental F_z', as shown in **Fig. 15**, is compared with the computational result of Fig. 12. Both the phase and the amplitude of the computational result are the same as the experimental result. Moreover the waveform is also the same, except for the high order components of the vibration.

4. Analysis and Consideration

4. 1 Analysis Results of Actual Case

Figure 16 shows two kind of computational F_z', applying different respective relative motions. The solid line shows the result utilizing all relative motions to simulate the actual motion using three rollers. The broken line shows the result using the pitching motion corresponding to the validation of the analysis model. Comparing both results, the principal characteristics of the waveforms are almost same, even though the phase is different. It can be inferred that the pitching motion is dominant in all relative motions.

Next, **Fig. 17** shows the rotational order tracking analysis for both results. The first and the third rotating order components appear clearly.

In the actual condition using three rollers, each phase angle of these components is different by 120 degrees
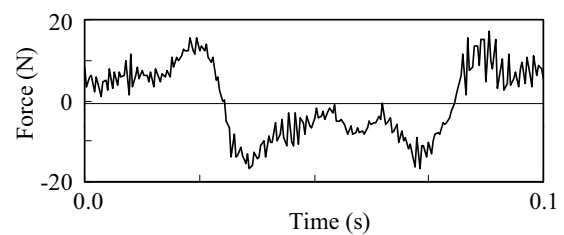

Fig. 13 Photograph of experimental apparatus for validation.

Fig. 15 Experimental result of modified thrust force F_z'.

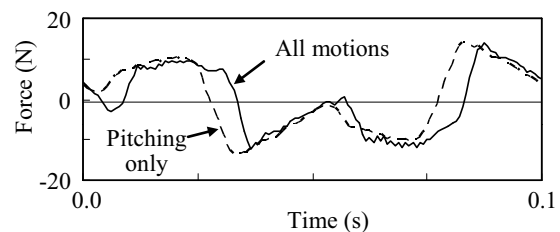**Fig. 14** Experimental result of pressing force ΔF_x and lateral force F_y.

Fig. 16 Computational result of modified thrust force F_z'.

because of the equally arranged grooves. Therefore, by summing together the three thrust forces, the first rotating order component is nearly zero and the third rotating order component is three times the amplitude of a case with one roller.[1]

4. 2 Factors Inducing Sliding Friction of Roller

As described in Section 1, the principal factor inducing the third rotating order component of the thrust force is the sliding friction between the roller and the groove. The contribution of this friction was confirmed by a parameter study of contact regions and friction types. As a result, it is found that this sliding friction accounts for 92% of the effective value of the third rotating order component when using all relative motions.

Here, assuming that the friction defined in the analysis model is limited only to this sliding friction, the influence of each relative motion is researched. **Fig. 18** shows F_z' in a case where each relative motion is added to the basic pitch motion. The waveform of the case adding the rolling motion corresponds to the case using all relative motions. The following section therefore discusses the sliding friction based on the pitching and rolling motions. It also discusses the sliding friction indirectly derived from the locus of the point of contact.

4. 2. 1 Sliding Caused by Pitching Motion

The traveling direction of the roller is regulated by the groove, but the rotating direction of the roller changes according to the pitching motion. Therefore, these directions do not correspond. The angular difference between the traveling direction and the rotating direction is equal to the pitching angle φ, and the maximum angular difference is same as the joint angle θ, as shown in **Fig. 19**. The sliding direction of the roller is orthogonal to the rotating direction and

turns to the same side of the traveling direction. Here, using Eq. (2), the displacement of the z direction is defined as follows.

$$z = s \tan\varphi \approx s\,\theta\,\sin\omega t \cdots\cdots\cdots\cdots\cdots\cdots (18)$$

Using this equation, the sliding velocity of the roller on the groove is defined as follows.

$$v_1 = \frac{dz}{dt}\sin\varphi = \frac{s\,\omega\,\theta^2}{2}\sin 2\omega t \cdots\cdots\cdots (19)$$
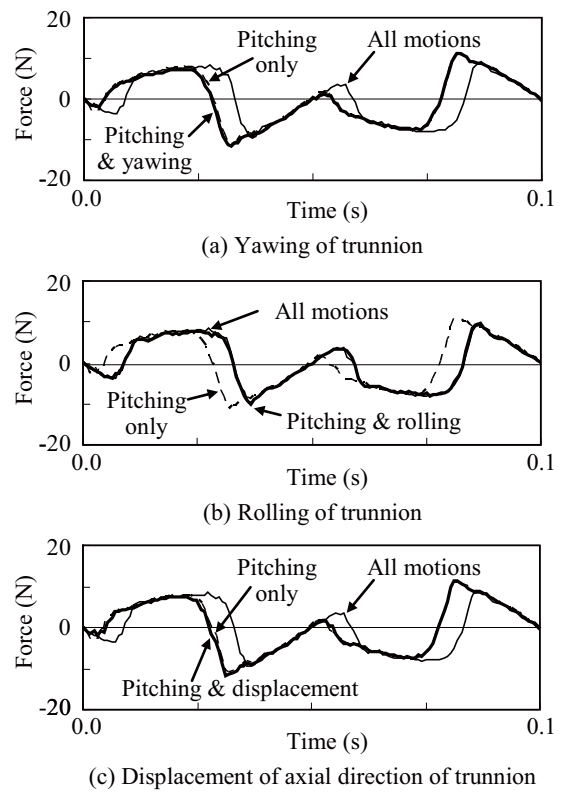

(a) Yawing of trunnion

(b) Rolling of trunnion

(c) Displacement of axial direction of trunnion

Fig. 18 Relations between relative motions and modified thrust force F_z'.
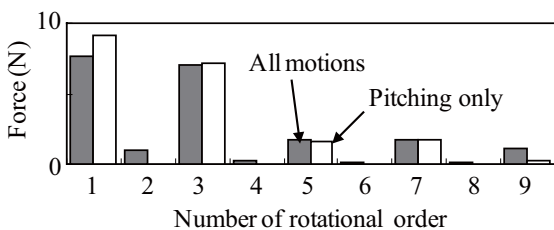

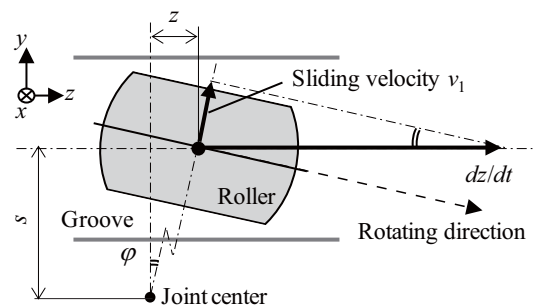**Fig. 17** Result of rotational order tracking analysis.

Fig. 19 Sliding velocity for pitching motion of roller.

4. 2. 2 Sliding Caused by Rolling Motion

The roller rotates relatively around the axis of the groove direction because of the rolling motion caused by the eccentric revolution of the spider, and slides in the opposite direction to v_1. If the radius of the roller is r, the sliding velocity is defined as follows.

$$v_2 = -r\frac{d\xi}{dt} = -r\omega\frac{1-\cos\theta}{\cos\theta}\cos 2\omega t \cdots\cdots (20)$$

4. 2. 3 Sliding Caused by Traverse of Point of Contact

Figure 20 shows the locus of the point of contact on the zy plane. The locus, which resembles the character "∞", shows that the roller does not always touch the bottom of the groove, but instead makes contact at a slope part of the groove. Sliding between the roller and the groove is generated when the roller, which has a degree of freedom to the axial direction, crosses the bottom of the groove from one slope to the other as shown by the arrows in Fig. 20. Since the sliding velocity of the y direction is explained in the following section, the reason for the contact at the slope is discussed below.

Figure 21 shows the force acting from the roller to the groove. The sliding direction of the roller is orthogonal to the rotating direction and is defined as positive in the case going away from the joint center. It is assumed that the components of the sliding friction f_t are f_{ty} and f_{tz} (f_{tx} is neglected because of a small value) and the components of the contact force f_n are f_{nx} and f_{ny} ($f_{nz} = 0$). F_x, F_y, and F_z mentioned above are defined as follows.

$$F_x = f_{nx} \cdots\cdots\cdots\cdots\cdots\cdots\cdots\cdots (21)$$

$$F_y = -f_{ny} + f_{ty} \cdots\cdots\cdots\cdots\cdots\cdots (22)$$

$$F_z = f_{tz} \cdots\cdots\cdots\cdots\cdots\cdots\cdots\cdots (23)$$

Here, it is important that F_y is related to f_n and f_t. Considering the balance of forces acting on the roller, the reaction force of F_y is equal to the sum of the y direction forces received from the needle rollers. Since these y direction forces almost all generate by the sliding friction between the needle rollers and the inside surface of the roller, F_y is approximated as zero by applying the definition of the friction mentioned above (only considering the friction between the roller and the groove). Therefore, the point of contact is located in the position of the slope which satisfies the formula $f_{ny} \approx f_{ty}$. Here, in the case where all friction is considered, it is inferred that the locus of the point of contact widens in the direction of the slope, by deriving $f_{ny} > f_{ty}$ from $F_y < 0$.

4. 2. 4 Validation

Figure 22 shows v_1, v_2, the sliding velocity of the traverse of the point of contact, and the combined velocity of these three velocities. Here, f_t is calculated by multiplying the initial pressing force by the friction coefficient (considering the function shown in Fig. 8) in accordance with this combined velocity, and is converted into f_{tz}, that is, F_z. **Figure 23** shows F_z and F_z' computed by the analysis model. Since the
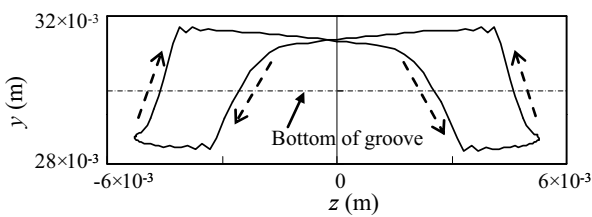

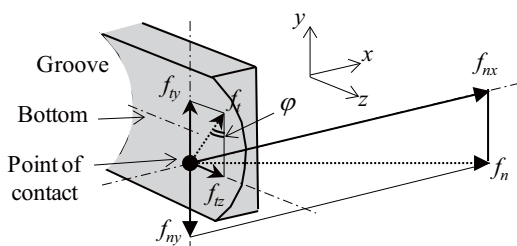**Fig. 20** Locus of point of contact on groove.

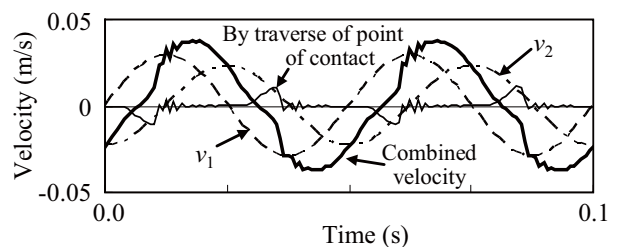**Fig. 21** Schematic of forces acting from roller to groove.

Fig. 22 Three sliding velocities and combined velocity.

characteristics of the waveforms of these results almost correspond, it can be inferred that the factor inducing the sliding friction of the roller is appropriate.

4.3 Reason Inducing Third Rotating Order Component of Thrust Force

Omitting the relative velocity by the traverse of the point of contact, the sliding velocity V is simplified as the sum of v_1 and v_2, and is defined by

$$V = A \sin 2\omega t + B \cos 2\omega t , \quad \cdots \cdots \cdots \cdots (24)$$

where the amplitude A and B are defined as

$$A = \frac{s\,\omega\,\theta^2}{2} , \; B = -r\,\omega\,\frac{1-\cos\theta}{\cos\theta} ,$$

and α is a angle satisfying the following equations:

$$\sin\alpha = \frac{B}{\sqrt{A^2 + B^2}}, \; \cos\alpha = \frac{A}{\sqrt{A^2 + B^2}} \; .$$

Calculating f_t with respect to this case, the waveform is shown as **Fig. 24**. The principal component is the second rotating order component as follows.

$$f_{t\,2nd} = C \sin(2\omega t + \alpha) \quad \cdots \cdots \cdots \cdots \cdots (25)$$

where C is the amplitude. Next, the z direction of $f_{t\,2nd}$ is shown as

$$f_{tz\,2nd} = f_{t\,2nd} \sin\varphi \approx C\,\theta \sin(2\omega t + \alpha) \sin\omega t . \\ \cdots \cdots \cdots \cdots \cdots \cdots (26)$$

This formula is expanded and arranged as follows.

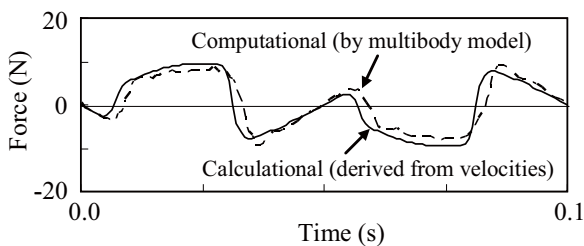$$f_{tz\,2nd} = C\,\theta / 2 \left[-\sin(\omega t + \beta) + \sin(3\omega t + \beta) \right] , \\ \cdots \cdots \cdots \cdots \cdots \cdots (27)$$

where β is the angle satisfying the following equations:

$$\sin\beta = \frac{-A}{\sqrt{A^2 + B^2}}, \; \cos\beta = \frac{B}{\sqrt{A^2 + B^2}} \; .$$

The reason that f_{tz}, namely, F_z includes the third rotating order component is that the combination of the first and the third rotating order components is derived by transforming f_t, which consists of the second rotating order component, into the component of the z direction. Here this study clarifies that the inducement of the third rotating order component of the thrust force is not related to a structure consisting of three rollers and grooves but is a phenomenon found with one roller and groove.

5. Conclusions

In this research, an analysis model of a tripod constant velocity joint was constructed by the principal parts for one roller and groove and was validated by comparison with an experiment performed under the same conditions. The computational result derived by this model was studied in detail, and the mechanism inducing the thrust force was clarified. These results are summarized as follows.

(1) The following principal factors cause sliding friction between the roller and the groove. (a) The traveling direction of the roller is regulated by the groove, but the rotating direction of the roller changes according to the pitching motion. Therefore, these directions do not correspond. (b) The roller rotates relatively around the axis of the groove direction because of the rolling motion caused by the eccentric revolution of the spider. (c) The roller does not always touch the bottom of the groove but contacts at a slope part of the groove, and the locus, which resembles the character "∞" is formed in accordance with the balance of forces acting on the roller. Relative displacement occurs between the roller and the groove when the
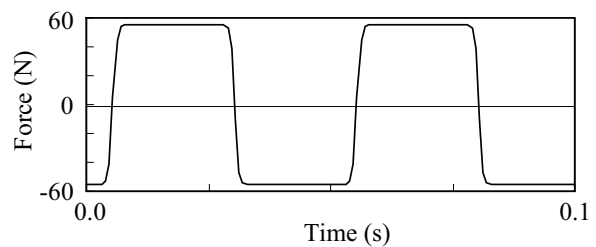

Fig. 23 Validation of thrust force based on three velocities.

Fig. 24 Sliding friction by velocities v_1 and v_2.

roller, which has a degree of freedom to the axial direction, crosses the bottom of the groove from one slope to the other.

(2) The component of the groove direction of this sliding friction becomes the thrust force. When this friction, which consists of the second rotating order component is converted to the sine components of the pitching angle, this waveform mainly forms the combination of the first and the third rotating order components. Since each phase angle of these components is different by one third of the cycle in actual conditions using three rollers and grooves, the third rotating order component is three times the amplitude of a case using one roller, but the first rotating order component is found to be nearly zero by summing together the three thrust forces. Therefore, the principal factor of the thrust force is the third rotating order component.

References

(1) Sugiura, H., Matsunaga, T., Mizutani, Y., Ando, Y. and Kashiwagi, I., "Thrust Force Analysis of Tripod Constant Velocity Joint Using Multibody Model", *R&D Review of Toyota CRDL*, Vol. 42, No. 2 (2011), pp. 55-64.

(2) Kimata, K., "Friction and Lubrication of Constant Velocity Joints", *Journal of Japanese Society of Tribologists*, Vol. 31, No. 10 (1986), pp. 697-702.

(3) Dodge, J. H. and Wagner, E. R., *Universal Joint and Driveshaft Design Manual* (1979), p. 131, SAE.

(4) Haug, E. J., *Computer-Aided Kinematics and Dynamics of Mechanical Systems : Basic Methods*, Vol. 1 (1989), pp. 218-229, Allyn and Bacon.

(5) Computer Aided Design Software, Inc. ed., *DADS Revision8.0 Reference Manual* (1997), Computer Aided Design Software, Inc.

(6) Okamoto, J., Nakayama, K. and Sato, M., *Introduction to Tribology* (in Japanese) (1990), p. 115, *Saiwai Syobo*.

(7) Brändlein, J., Eschmann, P., Hasbargen, L. and Weigand, K., *Ball and Roller Bearings : Third Edition* (1995), Wiley.

(8) Harris, T. A., *Rolling Bearing Analysis* (1966), p. 437, Wiley.

(9) Okamoto, J. and Nozawa, Y., *Needle Roller Bearings* (in Japanese) (1991), p. 111, *Koyo Seiko*.

Hideki Sugiura
  Research Fields:
    - Application of Multibody Dynamics
    - Development of Suspension Design Method
  Academic Societies:
    - The Japan Society of Mechanical Engineers
    - Society of Automotive Engineers of Japan
  Awards:
    - The Japan Society of Mechanical Engineers Design & Systems Conference 2008 Certificate of Merit for Excellence in Design & Systems Contest, 2008
    - The Japan Society of Mechanical Engineers Dynamics & Design Conference 2009 Best Presentation Award, 2010
    - The Japan Society of Mechanical Engineers Design & Systems Conference 2011 Certificate of Merit for Excellence in Design & Systems Contest, 2011

Yoshiteru Mizutani
  Research Fields:
    - Development of the Load Measurement Transducer
    - Test and Research on the Structural Strength of the Vehicle

Tsugiharu Matsunaga
  Research Field:
    - Automotive Hydraulic System
  Academic Societies:
    - The Japan Society of Mechanical Engineers
    - Society of Automotive Engineers of Japan

Yosei Ando*
  Research Field:
    - Development of Constant Velocity Joints

Isashi Kashiwagi*
  Research Field:
    - Development of Constant Velocity Joints
  Academic Society:
    - Society of Automotive Engineers of Japan

                                                    * JTEKT Corporation